# Systematic Error Reduction in UAV-Based Laser Scanning by Using RTS

André Cornelißen\*<sup>1</sup>, Ansgar Dreier<sup>1</sup>, Felix Esser<sup>1</sup>, Gereon Tombrink<sup>1</sup>, Lasse Klingbeil<sup>1</sup>, Heiner Kuhlmann<sup>1</sup>

<sup>1</sup> Institute of Geodesy and Geoinformation, University of Bonn, Germany

Keywords: UAV, Laserscanning, Trajectory Estimation, Factor Graph, Robotic Total Station

#### **Abstract**

In the last decades, Uncrewed Aerial Vehicles (UAV) with Light Detection and Ranging (LiDAR) sensors have become very popular for capturing high-resolution 3D-Point clouds, enabling the efficient measurement of large-scale objects in a short time. This is realized by fusing data from multiple sensors, usually Inertial Measurement Unit (IMU) and Global Navigation Satellite System (GNSS) to obtain the trajectory of the UAV and the LiDAR Scanner for point cloud generation.

A crucial part in this process is the absolute positioning with GNSS. Systematic errors can occur especially due to challenging GNSS conditions, regarding the number of satellites, their distribution and site-dependent effects. These errors have a direct influence on the point cloud quality.

The contribution of this paper is an extension of a UAV laser scanning system with a prism, that is continuously tracked using a Robotic Total Station (RTS). A factor graph-based trajectory estimation technique is used to fuse IMU and RTS data for a high-precise trajectory estimation to reduce systematic errors. The acquired data and a reference data set are used to evaluate our approach. The results show that point cloud misalignments can be reduced by integrating RTS data in the UAV trajectory estimation by up to  $6\ cm$ .

#### 1. Introduction

Uncrewed Aerial Vehicles (UAVs) equipped with LiDAR (Light Detection and Ranging) enable high-precision 3D point cloud generation, ensuring efficient and accurate spatial data acquisition. The most crucial part is to maintain accurate and reliable UAV positions and orientations. The most common approach to this challenge is to fuse observations from Global Navigation Satellite Systems (GNSS) with data from an Inertial Measurement Unit (IMU). GNSS positions can be affected by systematic deviations, caused by site-dependent effects, that are directly transferred to the point cloud, causing misalignments between multiple flight strips (Dreier et al., 2021). High precision applications, especially based on multiple and epoch-wise measurements, are highly affected by this problem.

One possible solution is to use strip adjustment methods (Glira et al., 2016). These align multiple flight strip point clouds to minimize systematic effects in the trajectory estimation, also the ones which are not necessarily caused by GNSS (Habib et al., 2008). However, multiple flight strips with sufficient overlap are inevitable for these methods. Although the different strips are adapted to be consistent to each other, systematic errors may still remain. Another approach is to extend the trajectory estimation by directly using the acquired laser scan data to reduce uncertainties within point clouds (Pöppl et al., 2023). This approach is similar to the strip adjustment, but it goes beyond point cloud level. The geometry of point clouds is not only used to shift and rotate the individual strip point clouds but also to improve the trajectory within the strips. This also allows for the estimation of the calibration parameters to obtain a more reliable solution.

A different approach is to directly improve the trajectory estimation by adapting or adding hardware or optimizing algorithms. One example, which is also the basis of this contribution, is to add a prism to the UAV set-up and use a Robotic Total Station (RTS) to track it over time and generate accurate position information with a potential higher accuracy than GNSS.

A comparable approach focuses on the angle measurement of two RTS, which are used to determine the continuous positions of an mobile mapping system (Kerekes and Schwieger, 2018). The use of two angle measurements can be beneficial over distance measurements because of a higher accuracy and sampling rate. The challenge of time synchronization between mobile mapping systems and RTS is addressed in Vogel and Hake (2024), while investigating reference trajectories. Using a prism that is tracked with high accuracy by a RTS, the GNSS receiver could potentially be replaced, and the accuracy of the resulting estimation can be improved, as shown in Thalmann and Neuner (2024). There, the prism positions in a local frame are fused with the IMU measurements using an error state Kalmanfilter (EKF). This enables high precision position and orientation estimation that outperforms GNSS/IMU fusion in multiple scenarios.

There are different methods to estimate a trajectory using multiple sensors. The most popular approaches are based on Kalman Filtering (Kalman, 1960) or Smoothing for offline processing, recursively computing the state of a system considering all sensor readings and their uncertainties. These methods are usually used in commercial GNSS/IMU processing software packages. Another method with increasing popularity is using factor graphs (Dellaert, 2012), in some communities also known as Dynamic Networks (Cucci and Skaloud, 2019). They consists of a graph-based structures which describes the functional model between sensor measurements and the estimated states, and they offer an effective way to formulate and solve the estimation process as a least-squares problem. They are very suitable for the integration of prism positions and are used in the presented work.

The contribution of this paper is the development and evaluation of an improved UAV laser scanning system. It is based on a prism attached to the platform, which is then tracked using an RTS with high positional accuracy. The prism positions then effectively replace GNSS data and thus the resulting systematic errors typically associated with GNSS-based trajectory estima-

tion. We use a factor graph approach to fuse the RTS data with IMU to estimate a trajectory. This improvement is evaluated at the trajectory and point cloud level. On trajectory level, we compare the RTS based trajectory positions with a GNSS based trajectory estimation. On point cloud level, we first focus on the consistency between repeated UAV point cloud acquisitions of the same area, and secondly on the comparison with an absolute terrestrial laser scanner (TLS) reference.

### 2. Materials and Methods

The following Section describes in Subsection 2.1 the pipeline for point cloud creation in UAV laser scanning. Subsection 2.2 presents the contribution of our work, the factor graph based trajectory estimation with additional RTS positions. Section 2.3 presents the sensor setup used and the processing of the data.

### 2.1 Direct georeferencing

To generate point clouds, the laser scanner measurements are combined with the trajectory parameters. This process is shown in Figure 1. First, the 2D profile scanner on the UAV generates measurements  $\mathbf{x}^s$  in the sensor frame (s). Second, these data are transformed into the body frame (b), using the system calibration, which consists of the bore-sight angle matrix  $\mathbf{R}^b_s$  and the lever-arm vector  $\mathbf{t}^b_s$ . Third, the trajectory parameters in the form of a translation  $\mathbf{t}^e_b$  and the three angles roll  $\phi$ , pitch  $\theta$  and yaw  $\psi$  at the time t of each scanner measurement are used to transform the scanner data to a global reference frame. The corresponding functional model of direct georeferencing for the point in time t is shown in Equation 1. While the system calibration is fixed, the other components are time dependent.

$$\mathbf{x}^{e}(t) = \mathbf{t}_{b}^{e}(t) + \mathbf{R}_{n}^{e}(t)\mathbf{R}_{b}^{n}(t)\left(\mathbf{t}_{s}^{b} + \mathbf{R}_{s}^{b}\mathbf{x}^{s}(t)\right)$$
(1)

## 2.2 Factor graph-based trajectory estimation

Creating consistent point clouds with the direct georeferencing as shown in Figure 1 needs the trajectory of the UAV to be estimated with high precision. The trajectory consists of i navigation states  $\mathbf{n}_i$  containing the position, velocity, and orientation of the system in a global reference frame e, defined with

To compensate for time-dependent systematic deviations in the IMU observations, the estimation problem also contains the acceleration and gyroscope bias of the IMU (Groves, 2013), defined with

$$\mathbf{b}_{j} = \left[ b_{a_{x,j}}, b_{a_{y,j}} b_{a_{z,j}} b_{\omega_{x,j}}, b_{\omega_{y,j}} b_{\omega_{z,j}} \right]^{T}$$
 (3)

indexed with j. The set of all states to be estimated is summarized by

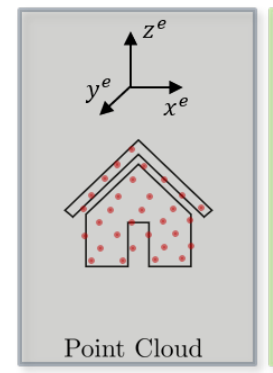
$$\mathcal{V}_K = \left\{ \mathcal{X} = \left\{ \mathbf{x}_i^e \right\}_{i=0}^N, \mathcal{B} = \left\{ \mathbf{b}_j \right\}_{j=0}^M \right\}$$
 (4)

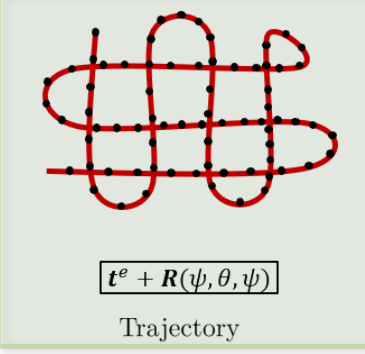
where N and M highlight the total number of navigation states and IMU bias variables. To estimate the variables of Equation 4, absolute position measurements are often fused with the relative IMU observations using Kalman filter algorithms, but modern methods such as factor graphs are also commonly used (Dellaert, 2012). In this work, we use a factor graph-based approach, as it enables both a flexible integration of new sensor observations and smooth trajectory estimates.

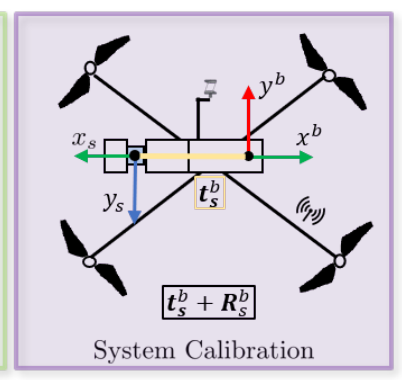
Factor graphs are an illustrative presentation of the state optimization problem and consist of nodes and factors. The nodes represent the unknown variables of the trajectory and the IMU bias, and the factors describe the functional relationship between the sensor observations and unknown variables. Figure 2 shows the factor graph of our estimation problem, including factors for the sensor measurements of the RTS, GNSS and IMU and the variables for the navigation states and bias variables. Assuming the normal distribution for the sensor observation, the parameter estimation problem can be written as a least-squares optimization problem, see Eq. 5, where the functions f are non-linear error functions of the sensor measurements and unknown parameters  $\mathcal{V}_K$ . To obtain the parameters in a least-squares adjustment, the Jacobians of the error functions are computed to set up a normal equation system that can be solved to estimate the unknown variables. In the following, the error functions of our factor graph are introduced, followed by the description of the least-squares optimization.

The IMU factor  $f_{ij}^{IMU}(\mathbf{n}_i,\mathbf{n}_j,\mathbf{b}_q,\mathbf{z}_i^{IMU})$  describes the error function of the process model. It depends on the consecutive trajectory states  $\mathbf{n}_i$  and  $\mathbf{n}_j$ , the bias  $\mathbf{b}_q$  and the IMU measurements  $\mathbf{z}_i^{IMU} = \{\mathbf{a}_i, \boldsymbol{\omega}_i\}$ . The measured specific force

$$\mathbf{n}_{i}^{e} = \left[t_{x,i}^{e}, t_{y,i}^{e}, t_{z,i}^{e}, v_{x,i}^{e}, v_{y,i}^{e}, v_{z,i}^{e}, \phi_{i}^{e}, \theta_{i}^{e}, \psi_{i}^{e}\right]^{T}.$$
 (2)







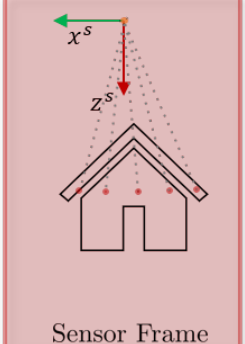


Figure 1. Direct georeferencing pipeline, that transforms laser scan data into a global reference frame.

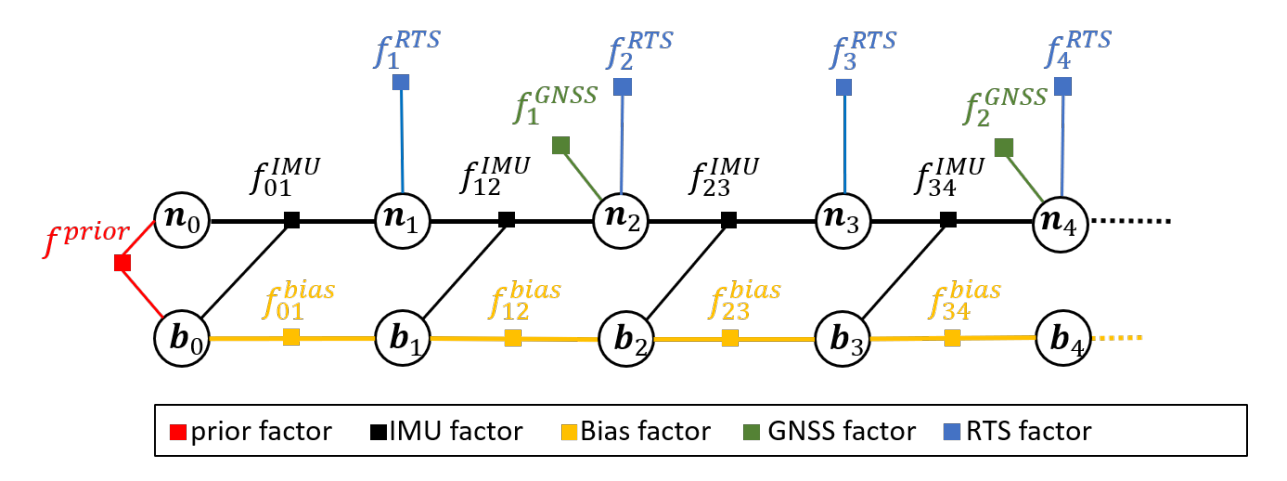


Figure 2. Factor graph representation of the trajectory estimation.

$$\mathcal{V}_{K}^{*} = \arg\min_{\mathcal{V}_{K}} \left\{ \sum_{i=0, j=i+1}^{K} \|f_{ij}^{\text{IMU}}\|_{\mathbf{\Sigma}_{ij}}^{2} + \sum_{q=0}^{Q} \|f_{q}^{\text{bias}}\|_{\mathbf{\Sigma}_{(q-1)q}}^{2} + \sum_{q=1}^{G} \|f_{g}^{\text{GNSS}}\|_{\mathbf{\Sigma}_{pp}}^{2} + \sum_{h=1}^{H} \|f_{h}^{\text{RTS}} \right\}.$$
 (5)

$$\mathbf{a}_{i} = [a_{x,i}, \ a_{y,i}, \ a_{z,i}]^{T} \tag{6}$$

and the angular velocity

$$\boldsymbol{\omega}_i = \left[\omega_{x,i}, \ \omega_{y,i}, \ \omega_{z,i}\right]^T \tag{7}$$

are used to propagate the navigation state  $n_i$  in time by integration. Since the update rate of IMU is typically very high, so-called pre-integrated measurements are used as described in Kaess et al. (2012) to reduce the computational cost. The position factor  $f_i^{Pos}(\mathbf{n}_i, \mathbf{z}_i^{Pos})$  computes the error between the predicted and the observed position measurement, while taking into account the lever-arm between the GNSS antenna and the body frame. The absolute position measurement  $\mathbf{z}_i^{Pos}$  can be both the GNSS measurement  $\mathbf{z_g}^{GNSS}$  or RTS measurement  $\mathbf{z}_h^{RTS}$ . This results in the GNSS factor  $f_g^{GNSS}(\mathbf{n}_g, \mathbf{z}_g^{GNSS})$  and the RTS factor  $f_h^{RTS}(\mathbf{n}_h, \mathbf{z}_h^{RTS})$ , where the indices g and h refer to the specific time steps corresponding to their associated navigation states. The IMU bias factor  $f_q^{bias}(\mathbf{b}_{q-1}, \mathbf{b}_q)$  models the temporal changes of the biases as a random walk process between two time steps q-1 and q. For more details about the bias factor, we refer to Kaess et al. (2012). The prior factor  $f^{\text{prior}}$  contains start values for the navigation state  $n_0$  and the priors on the bias variables  $b_0$ . The factors are used to formulate the least squares optimization representation in Equation 5. For the optimization, the factor nodes are linearized, and a system of normal equations is constructed. Using the error functions, the pose and bias parameters are estimated through global optimization. For parameter optimization, we use the incremental smoothing and mapping algorithm (Kaess et al., 2012) implemented in the 'GTSAM' library (Dellaert, 2012), as it efficiently optimizes the minimization problem of Eq. 5.

### 2.3 Measurement Platform and Data Processing

The UAV laser scanning system is manufactured by RIEGL (RIEGL, 2021). The IMU (Applanix APX20-UAV) is micro-electromechanical system (MEMS) based and consists of two triaxial sensors: an accelerometer to measure acceleration and a gyroscope to capture angular velocities. It has an update rate



Figure 3. Sensor setup with the additional Leica 360° prism.

of 200 Hz and is located behind the scanner, as shown in Figure 3. The raw IMU data is later used to estimate the trajectory. The APX-20 UAV also includes a built-in GNSS receiver. The antenna is located on top of the drone and mounted on a strut. The GNSS observations are processed in the software Applanix POSpac using data from a reference station for the baseline processing, creating output with a rate of 1 Hz and the typical accuracy of several centimeters. These positions are used for comparison and evaluation purposes further below.

The LiDAR sensor is a RIEGL mini-VUX, which is a 2D light-weight high-precision profile scanner. It measures on a  $360^{\circ}$  field of view with an accuracy of 1.5~cm at a distance of 50~m (RIEGL, 2021). It is mounted on the front of the UAV.

A Leica  $360^{\circ}$ -mini prism is attached to the bottom of the IMU (see Figure 3) and is tracked by the RTS (Figure 5). The RTS is a Leica TS60, which offers a tracking accuracy of  $3\ mm+1\ ppm$  (Leica Geosystems AG, 2016). In addition, the accuracy of the prism has to be taken into account, which is at  $1.5\ mm$  (Leica Geosystems AG, 2025). Empirical investigations indicate a standard deviation around  $1.5\ mm$  of the RTS and prism combination. To successfully integrate the RTS measurements into trajectory estimation, all involved sensors must be synchronized. The IMU and LiDAR data are recorded on the drone itself and refer to UTC-time. For the RTS data, we use a GPS-synchronized Raspberry Pi single board computer, which has already been used in Tombrink et al. (2025). This provides every RTS measurement with a GPS time

stamp. Taking leap seconds into account, we convert these time stamps to UTC-time, ensuring that all sensors involved refer to the same time system.

The position and orientation of the RTS is georeferenced using standard geodetic procedures such as resection. The local RTS polar measurement angles and distances are thus transformed into coordinates, which are given in the same coordinate system as the GNSS. The RTS based prism coordinates are now combined with the IMU data using the factor graph based algorithm as described in section 2.2. The trajectory, the previously determined system calibration parameters and the scanner data are then integrated to generate a georeferenced point cloud as described in section 2.1, using the 'Orientation and Processing of Airborne Laser Scanning data (OPALS)' toolbox (Pfeifer et al., 2014).

#### 3. Experiments

We performed a measurement and evaluated the results to demonstrate the general functionality of the system and its improved performance with respect to a GNSS-based solution.

### 3.1 Measurement Setup

The measurement data were collected at a geodetic research campus. The site contains a reference environment for mobile sensing systems (Heinz et al., 2020), which includes a very accurate geodetic network, several concrete pillars, a set of ground and wall mounted target points, as well as several buildings and structures, which are accurately scanned using terrestrial static scanners. As shown in Figure 5, the RTS is attached to a pillar with known coordinates. It is connected to a Raspberry Pi computer for control, data readout and data synchronization. It is very important to operate the drone in the line of sight between RTS and prisms, to receive continuous reliable data. This of course limits the flexibility of UAV laser scanning and the usability of this approach and must be taken into account. We performed four times the same flight line, parallel to the long wall of a building, two times in each direction. The resulting point cloud can be seen in Figure 4. We calculated two different trajectory solutions, both using the factor graph based estimation algorithm as described in section 2.2. One solution uses the GNSS positions from the antenna on the UAV in combination with the IMU data, and the other ones uses the prism positions and the IMU. These trajectory solutions are then fed into OPALS to generate two different point clouds of the test environment.



Figure 5. Leica TS 60 (left), on a precisely coordinated pillar tracking the UAV(right).

#### 3.2 Evaluation

We evaluate the results on three ways. One is by comparing the two trajectories directly, a second by analyzing the inner consistency between the different flight lines, and a third is by comparing the resulting point cloud with previously recorded reference cloud.

**3.2.1 Trajectory Level** To evaluate the trajectories we show the position differences between the GNSS-based and the RTSbased trajectory in Figure 6. The differences for all directions are in a the range of  $\pm 5$  cm. However, the deviations in North and East are between -2 and 2 cm and clearly smaller than in the height direction.It is not clear, where exactly the deviations come from and which of the two options is correct. However, we can already see that the height component has more systematic deviations, which is also what we expect generally from GNSS-based position measurements. We also see, that the North and East deviations are less systematic and also within the range of the expected GNSS deviations. For all directions, possible system calibration uncertainties, for example in the lever arm between the antenna or the prism and the IMU, have an influence on the result. To further analyze the differences we use the point clouds, generated with the trajectories and the scanner readings. Due to clear significance of the height component, we also focus on this during the following evaluation.

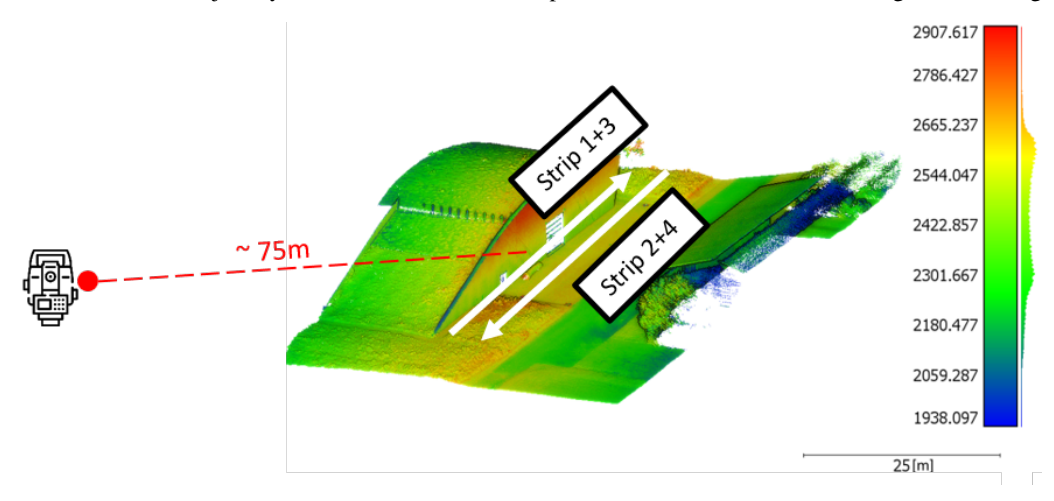


Figure 4. Point cloud calculated using the RTS positions, colored by intensity. The white arrows show the flight lines and the approximate position of the RTS is marked.

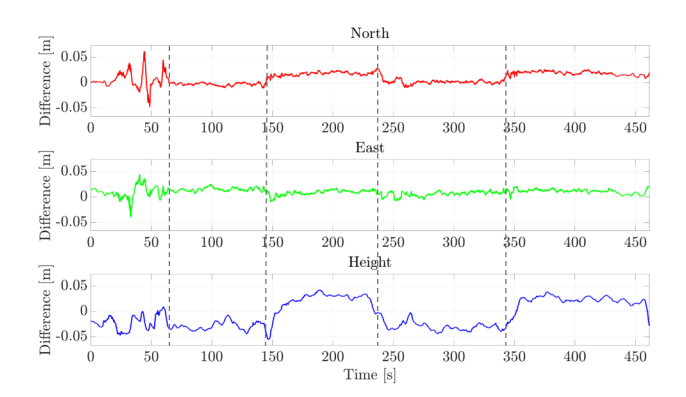
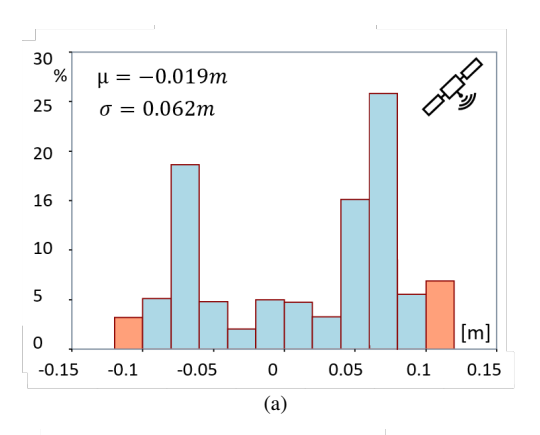


Figure 6. Position differences between the GNSS based and the RTS based trajectory, the dotted vertical line separates single flight strips.

**3.2.2 Point Cloud Level** The following paragraphs focus on the evaluation on the point cloud level. They are divided into the analysis of the consistency of the different flight strips and the absolute accuracy using a reference TLS scan.

Consistency We generated a digital height model of the environment for each of the eight flight lines using OPALS (Pfeifer et al., 2014) and plottet the differences between the models in a single plot (see Figure 7). The differences are color-coded on a scale from -10 to 10~cm. The area of interest is the area in front of the building. The left part of the Figure is the GNSS-based point cloud and the right part is the RTS-based point cloud difference map. The height differences on the left in Figure 7 show that the GNSS based flight strips point clouds differ by a different but constant offsets. This offset changes with every flight strip between -6 and 8~cm on the ground.

We also see differences in the vegetated roofs and the green verge, because the vegetation distorts the results. These effects therefore also occur in the RTS-based point cloud. However, in non-vegetation areas there are no systematic offsets between the flight strips visible for the RTS-based clouds. The visual results are supported by the histograms in Figure 8, that show the distribution of height differences in the point clouds occurring between the flight strips. Especially the standard deviation of the RTS based point cloud, which is smaller than the accuracy of the scanner, shows the significant improvement of the consistency when using RTS positions.



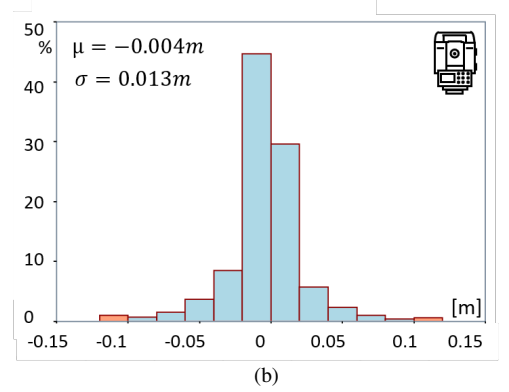


Figure 8. Histogram of point cloud height differences between different flight strips. a) GNSS-based trajectory, b) RTS-based trajectory.

Figure 9 shows the differences between individual flight strip for the case of the GNSS-based point clouds. Although it is very difficult to analyze the exact origin of the offsets, which is also beyond the scope of this paper, it is interesting to observe, that the offset remains somewhat constant during every flight strip and that the flight strips with the same flight direction also have a similar offset (see b and e). This is also consistent with the trajectory level evaluation in Figure 6.



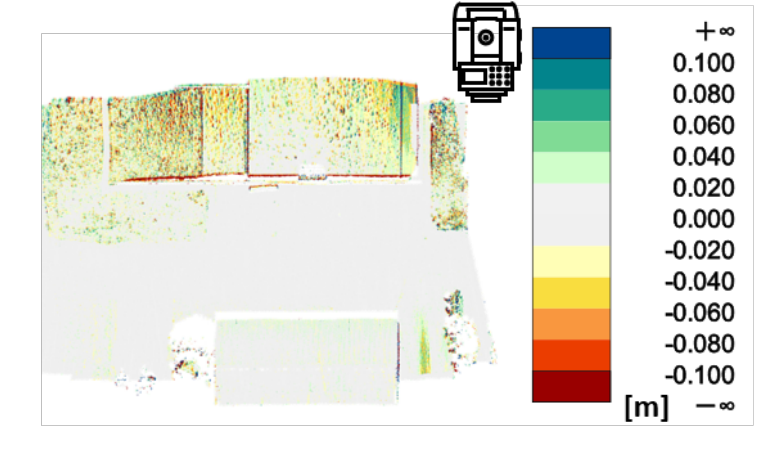


Figure 7. Pairwise height differences between multiple measured GNSS trajectory based point clouds (left, symbol: satellite) and multiple RTS trajectory based point clouds (right, symbol: total station).

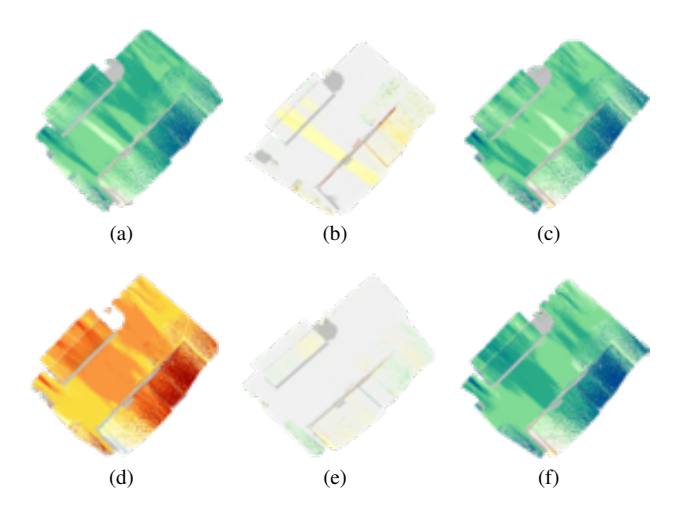
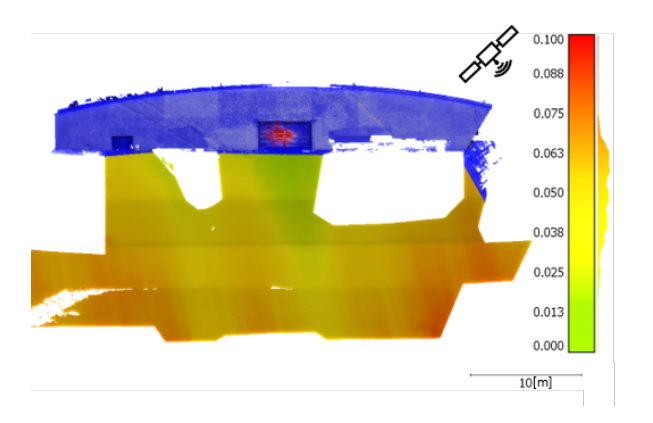


Figure 9. Differences between GNSS based flight strips: (a) Strip 1 vs. 2, (b) Strip 1 vs. 3, (c) Strip 1 vs. 4, (d) Strip 2 vs. 3, (e) Strip 2 vs. 4, (f) Strip 3 vs. 4, scale in Figure 7.

Absolute Accuracy Figure 10 shows the M3C2 (Lague et al., 2013) differences between a TLS point cloud and two UAV point clouds. A Leica ScanStation P50 was used to record a reference TLS point cloud. It was georeferenced using scan targets, whose coordinates where very accurately determined using a geodetic network. Therefore, we expect a significantly higher accuracy compared to a kinematically recorded point cloud. The reference TLS point cloud is now compared to both UAV point clouds of the first single flight strip.

The point cloud on the left is based on the trajectory estimated with GNSS positions, and the point cloud on the right is based on RTS positions. The slightly blue colored front of the building has been added to generate the context for the data, but has not been considered in the comparison. The area of interest for the comparison is shown as the dark blue area in front of the building in figure 11 Some parts are cut out, because the TLS point cloud was staggered in time to the UAV point cloud, which led to the appearance of moving vehicles in the investigated area, which were not in both point clouds. The M3C2 differences are colored in the point cloud according to the scale on the right to each point cloud, ranging from 0 and 8 cm. We chose to only show a single flight strip in this analysis, because the difference between the strips has been already shown before and too many inconsistent data would have made an interpretation of the results more difficult.



The differences computed with the GNSS based point cloud vary between 2.5 and  $7.5\ cm$ . A maximum can be seen around  $6.3\ cm$ . More peaks appear around 4.5cm. That shows an unsteady distribution, which can also be seen in the point cloud on the left, where variations in the differences along the direction of flight are visible. Of course, the differences would look different, when choosing a different flight strip.

The same scan data were used in the right part of the Fig-

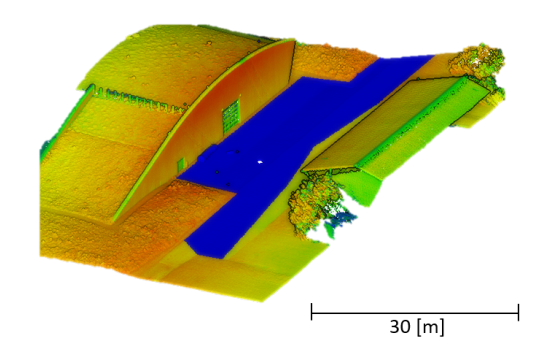


Figure 11. Measurement environment. Blue area shows M3C2 comparison location.

ure, this time using the RTS-based trajectory. The deviations are in a smaller range between 1.3 and  $4\ cm$  with the most differences around 2.5 cm is visible. Contrary to the GNSSbased point cloud, there are no variations along the flight line. A very slight gradient is visible in the bottom right area perpendicular to the flight direction, which might be result of a boresight angle error or a systematic error in the roll angle of the trajectory estimation. The constant offset between the UAV based point clouds and the TLS based point clouds could have several reasons. An error in the z-component of the lever-arm between the scanner and the IMU or the prism influence the absolute height of the point cloud directly and cannot be detected by multiple measurements. In principle also other offsets in the geodetic network, the georeferencing of the RTS or in general the height system used here are possible. However, as this offset is constant and small over the whole measurement we do not consider it as a result of the method presented in this work. The results show the benefit of the use of RTS positions for UAV laser scanning. This benefit even occurs in environments with good GNSS conditions, like at our research site. Higher reliability of the trajectory and the point clouds with respect to absolute positions is confirmed, and smoother point clouds with fewer variations are created.

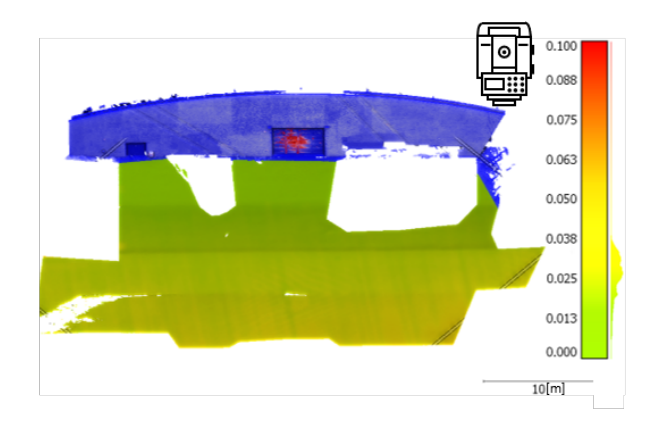


Figure 10. M3C2 distances from a single GNSS(left)- and a single RTS(right)-based point cloud strip to the TLS reference.

#### 4. Conclusion

In this paper, we presented an approach to increase the reliability of the trajectory estimation for UAV-based laser scanning. Our method extends the UAV platform by attaching a prism that can be precisely tracked using a ground-based RTS. This allows us to successfully increase the point cloud's inner and absolute accuracy. In comparison to a GNSS based approach, the inner consistency improved by up to 6 cm.

We implemented and evaluated our approach on trajectory and point cloud level and provided a comparison to a reference TLS point cloud. The experiments suggest that using an RTS is promising, especially in challenging GNSS environments such as a water dams and for applications where high-precision data are required.

Further research can improve the approach by using the Prism in combination with GNSS to support the estimation of the yaw. It is also possible to add another prism to the system, which is tracked by a different RTS to further optimize the yaw's accuracy. A case study in an environment with challenging GNSS conditions can further confirm the benefit of our approach.

### Acknowledgment

This research was partly funded by German Research Foundation (DFG) under grant number 490989047, DFG FOR 5455 "TLS-Defo".

#### References

Cucci, D. A., Skaloud, J., 2019. On raw inertial measurements in dynamic networks. *ISPRS Annals of the Photogrammetry, Remote Sensing and Spatial Information Sciences*, 4, 549–557.

Dellaert, F., 2012. Factor graphs and GTSAM: A hands-on introduction. *Georgia Institute of Technology, Tech. Rep*, 2, 4.

Dreier, A., Janßen, J., Kuhlmann, H., Klingbeil, L., 2021. Quality analysis of direct georeferencing in aspects of absolute accuracy and precision for a UAV-based laser scanning system. *Remote Sensing*, 13(18), 3564.

Glira, P., Pfeifer, N., Mandlburger, G., 2016. Rigorous strip adjustment of UAV-based laserscanning data including time-dependent correction of trajectory errors. *Photogrammetric Engineering & Remote Sensing*, 82(12), 945–954.

Groves, P., 2013.

Habib, A., Kersting, A., Ruifang, Z., Al-Durgham, M., Kim, C., Lee, D., 2008. LiDAR strip adjustment using conjugate linear features in overlapping strips. *Proceedings of International Archives of the Photogrammetry, Remote Sensing and Spatial Information Sciences*, 385–390.

Heinz, E., Holst, C., Kuhlmann, H., Klingbeil, L., 2020. Design and Evaluation of a Permanently Installed Plane-Based Calibration Field for Mobile Laser Scanning Systems. *Remote Sensing*, 12(3). https://www.mdpi.com/2072-4292/12/3/555.

Kaess, M., Johannsson, H., Roberts, R., Ila, V., Leonard, J. J., Dellaert, F., 2012. iSAM2: Incremental smoothing and mapping using the Bayes tree. *The International Journal of Robotics Research*, 31(2), 216–235.

Kalman, R. E., 1960. A new approach to linear filtering and prediction problems.

Kerekes, G., Schwieger, V., 2018. Position determination of a moving reflector in real time by robotic total station angle measurements. *Proceedings of Geoprevi*.

Lague, D., Brodu, N., Leroux, J., 2013. Accurate 3D comparison of complex topography with terrestrial laser scanner: Application to the Rangitikei canyon (NZ). *ISPRS journal of photogrammetry and remote sensing*, 82, 10–26.

Leica Geosystems AG, 2016. Leica Nova MS60/TS60 User Manual. Heerbrugg, Switzerland. Version 1.0.

Leica Geosystems AG, 2025. Leica grz101 360° mini reflector. https://shop.leica-geosystems.com/de-DE/survey/accessory/geosystems/leica-grz101-360-degree-mini-reflector/buy. Product information, accessed June 2025.

Pfeifer, N., Mandlburger, G., Otepka, J., Karel, W., 2014. OPALS-A framework for Airborne Laser Scanning data analysis. *Computers, Environment and Urban Systems*, 45, 125–136.

Pöppl, F., Teufelsbauer, H., Ullrich, A., Pfeifer, N., 2023. Mobile Laser Scanning with Low-Cost Navigation Sensors: Compensating for Low-Grade Imu with Dual-Gnss and Tightly-Coupled LIDAR. *The International Archives of the Photogrammetry, Remote Sensing and Spatial Information Sciences*, 48, 403–410.

RIEGL, 2021. miniVUX-2UAV. http://www.riegl.com/uploads/tx\_pxpriegldownloads/RIEGL\_miniVUX-2UAV\_Datasheet\_2021-04-06.pdf. Ac-

RIEGL\_miniVUX-2UAV\_Datasheet\_2021-04-06.pdf. Accessed: November 16, 2024.

Thalmann, T., Neuner, H., 2024. Sensor fusion of robotic total station and inertial navigation system for 6DoF tracking applications. *Applied Geomatics*, 16(4), 933–949.

Tombrink, G., Dreier, A., Klingbeil, L., Kuhlmann, H., 2025. Spatio-temporal trajectory alignment for trajectory evaluation. *Journal of Applied Geodesy*, 19(2), 321–331. https://doi.org/10.1515/jag-2024-0040.

Vogel, S., Hake, F., 2024. Development of GPS time-based reference trajectories for quality assessment of multi-sensor systems. *Journal of Applied Geodesy*.